PCCP

Combined Effects of Emitter-Emitter and Emitter-Plasmonic Surface Separations Dictate Photoluminescence Enhancement in Plasmonic Field

Journal:	*Physical Chemistry Chemical Physics*
Manuscript ID	CP-ART-04-2022-001681.R1
Article Type:	Paper
Date Submitted by the Author:	15-Jun-2022
Complete List of Authors:	Thomas, Elizabeth Mariam; Indian Institute of Science Education and Research Thiruvananthapuram Cortes, Cristian L.; Argonne National Laboratory, Center for Nanoscale Materials Paul, Livin; Indian Institute of Science Education and Research Thiruvananthapuram Gray, Stephen; Argonne National Laboratory, Center for Nanoscale Materials Thomas, K.; Indian Institute of Science Education and Research Thiruvananthapuram

ARTICLE

Combined Effects of Emitter-Emitter and Emitter-Plasmonic Surface Separations Dictate Photoluminescence Enhancement in Plasmonic Field

Received 00th January 20xx,
Accepted 00th January 20xx

DOI: 10.1039/x0xx00000x

Elizabeth Mariam Thomas,[a] Cristian L. Cortes,[b] Livin Paul,[a] Stephen K. Gray,*[b] and K. George Thomas*[a]

The brightness of an emitter can be enhanced by metal-enhanced fluorescence, wherein the excitonic dipole couples with the electromagnetic field of the surface plasmon. Herein, we experimentally map the landscape of photoluminescence enhancement (EF_{exp}) of emitters in a plasmonic field as a function of emitter-emitter separation, s, and emitter-plasmon distance, t. We use Au nanoparticles overcoated with inert spacers as plasmonic systems and CdSe/ZnS quantum dot (QD) as an emitter bearing opposite surface charges. The t and s are varied by changing the spacer thickness and number density of QDs on the plasmonic surface, respectively. The electrostatic binding of emitters on the plasmonic surface and their number density are established by following the variation of zeta-potential. EF_{exp} is high, when t is short and s is large; nevertheless, decreases when emitter-emitter interaction dominates due to plasmon assisted nonradiative processes. In the absence of plasmonic field, enhancement observed is attributed to environment effects which is independent of s, confirming the role of electric field. Indeed, the distance dependence of EF_{exp} closely follows the decay of the plasmonic field on dilution of the emitter concentration on nanoparticles' surface (s = 18 nm). The QD-plasmon system is visualized in the framework of Thomson problem, and classical electrodynamics calculations give the trends in t and s dependence of the photoluminescence. Being the first report on the simultaneous dependence of t and s on plasmon-enhanced photoluminescence, the results presented herein will open newer opportunities in the design of hybrid systems with high brightness.

Introduction

Absorption and photoluminescence (PL) are the two extensively utilized analytical and spectroscopic methods for investigating the physical properties of molecules and materials. PL has several favourable features over absorption in real-life applications, particularly its sensitivity which is several orders of magnitude higher. Often, the PL intensity of an emitter is quantified by its quantum yield (QY). However, QY is independent of extinction coefficient at the excitation wavelength. Hence, a more meaningful quantity, denoted as brightness is used for practical applications. Being the product of QY and extinction coefficient at the excitation wavelength,[1] emitters with high brightness can be realized by enhancing the absorption coefficient of the emitter or/and its radiative rate.[2] One of the convenient strategies to improve the brightness of emitter is by placing it in the vicinity of a plasmonic material.[3] The electron cloud on the surface of plasmonic materials undergoes collective oscillation on excitation, generating a giant transition dipole moment with effective oscillator strengths of ~10^4-10^5 and an amplified electric field in its proximity.[4] Interaction of the plasmonic field with the oscillating dipole of the emitter can modify the excitation and emission processes of the latter.[5, 6] Indeed, a plasmonic nanoparticle can function as a nanoantenna at its localized surface plasmon resonance frequency, concentrating the field around it,[7-9] resulting in an increased excitation rate.[5, 10, 11] The plasmonic field can also promote a build-up in the local density of optical states,[12] ensuing an enhanced radiative rate. Thus, the plasmon-assisted enhancement in emission often called as metal-enhanced fluorescence (MEF)[13-15] has been an interesting topic since the first report by Drexhage.[16] Nonetheless, MEF is not as popular technique as its counterpart, surface enhanced Raman scattering (SERS),[17, 18] due to the undesirable deactivation channels leading to energy transfer (Förster resonance energy transfer,[19] surface energy transfer,[20] nanometal surface energy transfer,[19, 21] and so on) or electron transfer which quenches its PL.[22-24] The dynamics of these

[a] School of Chemistry, Indian Institute of Science Education and Research Thiruvananthapuram (IISER TVM), Vithura, Thiruvananthapuram, 695 551, India.
[b] Center for Nanoscale Materials, Argonne National Laboratory, Argonne, Illinois 60439, United States.

Electronic Supplementary Information (ESI) available: [details of any supplementary information available should be included here]. See DOI: 10.1039/x0xx00000x

competing processes –quenching *vs* enhancement of PL– is determined by various factors such as proximity of the emitter from the surface of plasmonic nanoparticle,[25-30] interaction between two neighbouring emitters placed on plasmonic surface,[31] orientation of transition dipole of the emitter,[32] size of plasmonic nanomaterial,[33, 34] spectral overlap between extinction spectra of plasmonic nanoparticle and absorption/PL spectra of emitter,[35-37] and so on.

The positioning of emitters in the plasmonic field can be achieved by binding them, either electrostatically or covalently,[38] on the surface of metal nanoparticles. The distance between the plasmonic surface and the emitters (represented as 't') decisively influences their PL characteristics which can be varied by (i) overcoating plasmonic nanoparticle with an inert shell (e.g., silica[31, 39] or a polymer[26, 40]) or (ii) functionalizing the surface with organic linkers.[41, 42] Critical parameters that influence emission quenching were identified by Mulvaney, Bach and co-workers as t, and the wavelength of fluorophore with respect to the plasmon resonance of Au nanoparticle.[43] Similarly, PL enhancement in the presence of a plasmonic field has been explored recently by various groups.[29, 31, 42, 44-54] Some of these reports include: (i) theoretical demonstration indicating that the enhancement is higher when one emitter is placed on metal surface compared to three emitters which drops with t;[44] (ii) experimental studies using IRDye800 bound on silica coated Au nanorods which exhibit a PL enhancement of 10-fold at t = 17 nm and when the dye-plasmon spectral overlap is maximum;[31] (iii) observations that the field enhancement is predominant over other nonradiative process when CdSe quantum dots (QDs) are densely packed on silica coated Au nanoparticles at large t;[45] (iv) investigation on the role of local orientation of dye molecule and local electric field intensity contour around Au nanorods in MEF using single-molecule fluorescence measurements[42] and (v) the role of excitation wavelength in MEF using CdSe QDs bound on Ag nanoparticles.[46] The density of emitters on the nanoparticles' surfaces which controls their nearest-neighbour separations (represented as 's') is yet another crucial factor affecting the PL characteristics. A significant decrease in PL was observed when separation between the dye molecules (IRDye 800) on the surface of silica coated Au nanoparticles is below 9 nm.[31] When placed on silica nanoparticles with s less than 10 nm, a decrease in PL intensity and lifetime of dye molecule (Atto 532) was reported, attributed to the nonradiative transfer of excitation energy.[43] Most of the above-mentioned literature reports[21, 25, 31, 42, 43] follow a covalent linkage strategy for binding emitters on plasmonic surface. However, uniform positioning of emitters on the surface is a challenge. In order to achieve covalent linkage, emitters having specific functional groups, which are capable of binding on to a plasmonic NP's surface are used. However, certain facets on the NP's surface exhibit selective reactivity towards such functional groups, e.g., thiol derivatives preferentially bind onto Au (111) surface,[55] which results in nonuniform binding of emitters. In this work, we adopt an electrostatic binding strategy by using negatively charged CdSe/ZnS QDs as emitters and positively charged Au nanoparticle as the plasmonic material to investigate how PL of an emitter is influenced by varying (i) its distance from the plasmonic surface (t) and (ii) the spacing between adjacent emitters (s). We hypothesize that since both entities being oppositely charged permit strong electrostatic binding of emitters on the plasmonic surface and these aspects are established by zeta-potential studies. At the same time, the repulsive interactions between the QDs position the electrostatically bound emitters in an equally spaced manner. Under this assumption, the hybrid system can be visualized within the canopy of the famous Thomson problem[56] wherein a spatial configuration of N like-charged species on a sphere achieves a configuration that minimizes the total electrostatic energy. Herein, we report a joint experimental and theoretical exploration on the landscape of PL enhancement of emitter(s) placed in plasmonic field as a function of QD-QD separations and spacer thicknesses. The comprehensive investigation presented is first of its kind wherein s and t are simultaneously varied to obtain the landscape of PL enhancement.

Results and discussion

CdSe quantum dots coated with ZnS having cysteine as capping ligand (denoted as CdSe/ZnS) and gold nanoparticles (AuNPs) having size 33 ± 3 nm are used as emitters and plasmonic platform, respectively. While studying the emission enhancement, it is advisable to excite the emitter far from the plasmon resonance to minimize the excitation enhancement. CdSe/ZnS is one of the most explored QDs having high colloidal stability. Its broad absorption permits excitation of the sample far from the plasmon resonance, thus minimizing the excitation enhancement. On the other hand, AuNPs offer chemical inertness and tunable surface plasmon resonances which can overlap with the optical characteristics of CdSe/ZnS (Fig. S1). The surface plasmon of AuNPs having size 33 ± 3 nm resonates at 527 nm (Fig. S2). The AuNP concentration is obtained using a power law expression for the dependence of extinction coefficient at the resonance maxima with particle diameter (ESI).[57] In the present case, AuNPs having such an intermediate size are chosen because light scattering is high in larger nanoparticles[58] while nonradiative energy transfer dominates in smaller ones leading to quenching of PL.[19, 33]

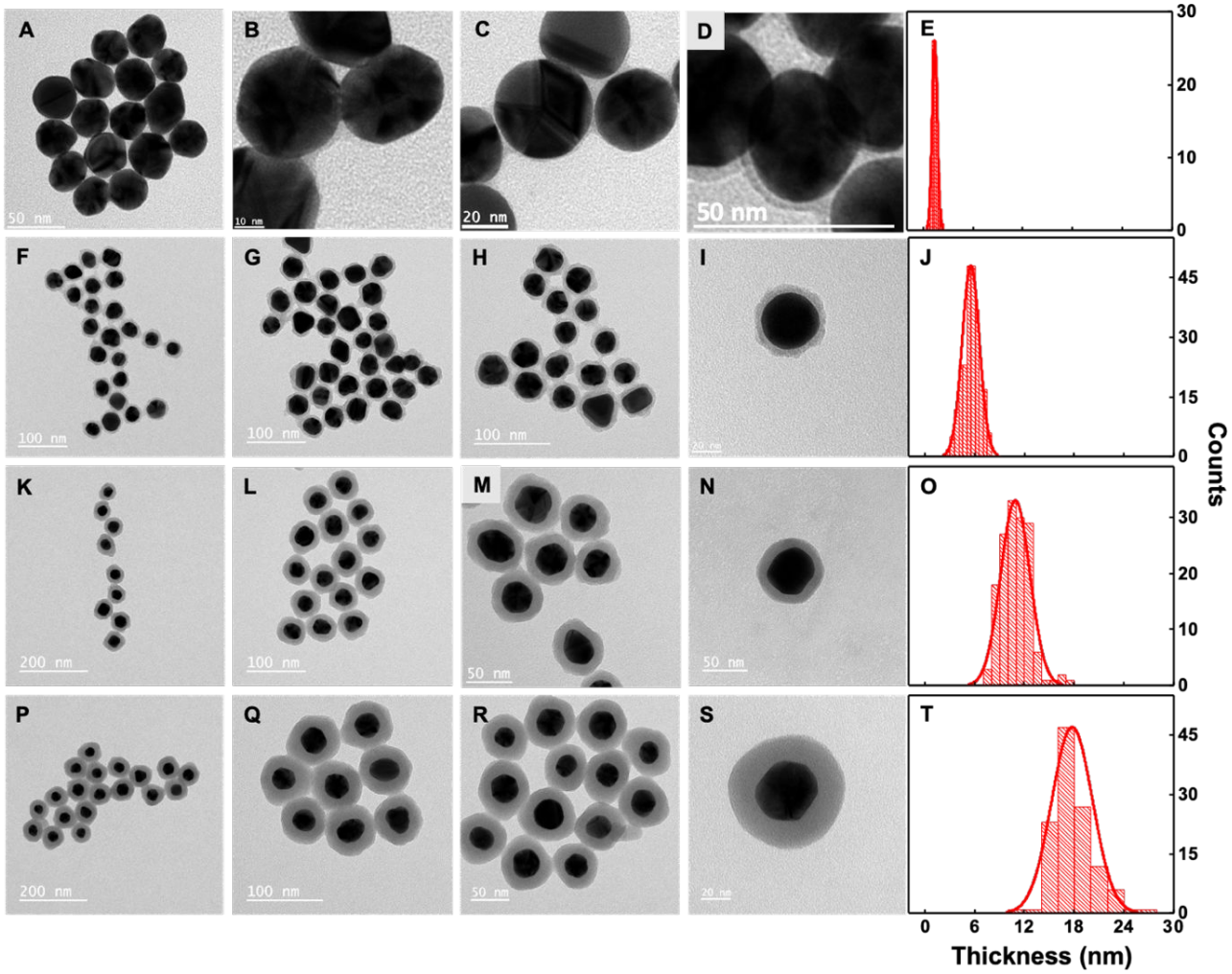

Fig. 1 TEM images of (A-D) Au(1.35), (F-I) Au-SiO_2(5.6), (K-N) Au-SiO_2(10.8), and (P-S) Au-SiO_2(17.3) at different magnifications. Histogram (E,J,O,T) of spacer thickness (E) Au(1.35), (J) Au-SiO_2(5.6), (O) Au-SiO_2(10.8) and (T) Au-SiO_2 (17.3). The histograms are determined by measuring the spacer thickness of around 100 particles.

Details of synthesis and characterization of nanoparticles (AuNPs and CdSe/ZnS) are provided in the Experimental Section and ESI. An optically inert silica spacer is utilized for varying the distance between the QD and AuNP. The silica coating of uniform thickness on AuNPs is accomplished by following the modified Stöber condensation reaction,[59] and the spacer thickness is tuned by changing the reaction time (Fig. 1). A red-shift in the extinction maximum of AuNP is observed on overcoating with silica due to the change in the dielectric environment. Both silica coated AuNPs (henceforth denoted as Au-SiO_2) and cysteine capped CdSe/ZnS possess negative surface charge (Fig. 2A,B). A thin polymer capping of poly(allylamine hydrochloride) (PAH) is employed on Au-SiO_2 to facilitate the electrostatic binding of QDs on the plasmonic surface (Fig. 2A). Upon binding of the polymer to the silica surface having negative surface charge, the zeta potential (ζ-potential) shifts from -28 mV to +48 mV. The thickness of the spacer after PAH coating is estimated from transmission electron microscopy (TEM) images and Au-SiO_2 is labelled with numerical extensions representing the thickness (in nm) of the spacer in parenthesis. Plasmonic systems with spacer thickness of ~5.6, ~10.8 and ~17.3 nm are represented as Au-SiO_2(5.6), Au-SiO_2(10.8) and Au-SiO_2(17.3), respectively. It is difficult to obtain uniform coating of silica with thickness <3 nm using Stöber condensation; hence we have directly coated PAH on AuNPs which yielded a spacer thickness of ~1.35 nm denoted as Au(1.35). Fig. 1 provides TEM images of Au(1.35), Au-SiO_2(5.6), Au-SiO_2(10.8) and Au-SiO_2(17.3), at different resolutions, along with histograms of spacer thicknesses. We have also synthesized silica nanoparticles (SiO_2 NP; radius of ~81 nm) with negative surface charge using a modified Stöber condensation reaction[60] to study the role of plasmonic field on MEF. TEM images of SiO_2 NPs along with size histogram is provided as Fig. S3. The diameter of SiO_2 NP is estimated from the histogram provided. The surface of SiO_2 NPs is made positive (+47.5 mV) by coating with PAH to facilitate the adsorption of negatively charged QDs. The particle concentration of SiO_2 NPs is determined using inductively coupled plasma-optical emission spectroscopy (ICP-OES) and TEM (Fig. S3). Details are provided in the ESI.

QD-bound plasmonic hybrids in water (3 mL) are prepared by the addition of negatively charged CdSe/ZnS to positively

Scheme 1. (A) Illustration of CdSe/ZnS electrostatically bound on Au nanoparticle having shell thickness (t) with QD-QD separation (s). The cross-sectional image of CdSe/ZnS bound on (B) Au nanoparticle and (C) silica nanoparticle.[a]

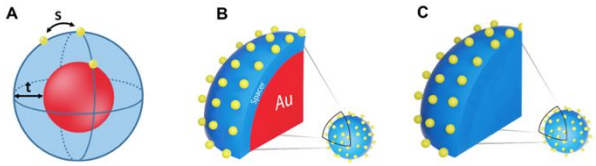

[a]The blue, red and yellow colors represent spacer, AuNP and QDs, respectively.

charged plasmonic systems with varying spacer in a quartz cuvette having path length of 1 cm. As mentioned in the introduction, rationale behind this design strategy involves two aspects: (i) the electrostatic force of attraction results in binding of CdSe/ZnS on the plasmonic surface and (ii) the electrostatic repulsion provides a uniform arrangement of nearly equally spaced QDs (*vide infra*). Herein, we investigate the emission of QDs bound on AuNPs by varying the spacer thickness (t) and the calculated separation between neighbouring quantum dots (s) on the surface of the plasmonic nanoparticle by changing the number density of CdSe/ZnS (Scheme 1A,B). The concentration of CdSe/ZnS required for a defined s at a given t is estimated by invoking the surface area of plasmonic nanoparticle (Table S1 and Scheme S1). The influence of plasmonic field on the emission of QDs is explored using CdSe/ZnS bound on SiO_2 NP which are devoid of AuNPs (ESI). An illustration of QD-bound plasmonic hybrid and SiO_2 NP are presented in Scheme 1.

The concentration of metal nanoparticles is kept constant (310 pM) for all the photophysical studies. The required concentration of CdSe/ZnS is added to plasmonic nanoparticles of varying shell thicknesses (Fig. 1) and allowed to equilibrate for 10 min before measurements. The extinction spectra of the CdSe/ZnS bound to Au(1.35), Au-SiO_2(5.6), Au-SiO_2(10.8) and Au-SiO_2(17.3) at different s values, overlap with the extinction spectra of the respective plasmonic NPs (Fig. S4) ruling out the possibility of any aggregation. The extinction spectra of CdSe/ZnS bound on SiO_2 NP at various QD-QD separations (s = 8, 13 and 18 nm) are provided as Fig. S5. Further we have followed time-dependent extinction spectrum of the hybrid system to confirm the colloidal stability. The extinction spectrum of the CdSe/ZnS bound on Au(1.35), measured as a function of time, remained same (Fig. S6A). Optical density at the extinction maximum (528 nm) and half-width at half-maximum, plotted as a function of time (Fig. S6B,C), also remained constant indicating that there are no changes in spectral features such as decrease in extinction or broadening of spectra. These results confirm the colloidal stability of the hybrid system which is further supported by high zeta potential values (*vide infra*).

QDs and plasmonic nanoparticles are in the same molar concentration range, however the extinction spectrum of the hybrid system is dominated by the contribution from the latter due to its larger extinction coefficient (ε = 4.82 x 10^9 $M^{-1}cm^{-1}$) compared to CdSe (ε = 1.95 x 10^5 $M^{-1}cm^{-1}$). Details of the estimation of ε is presented in the ESI. The binding of QDs to plasmonic nanoparticle surface is monitored by following the decrease in ζ-potential values of the hybrid systems. The ζ-potential becomes less positive on addition of CdSe/ZnS (-60 mV) to positively charged AuNPs (+52 mV – +59 mV) confirming the electrostatic binding. For example, the ζ-potential of Au(1.35) is estimated as +62 mV which decreased to +59 mV on addition of CdSe/ZnS (Table S2). On increasing the number density of CdSe/ZnS on the plasmonic nanoparticles, the ζ-potential value becomes less positive due to the scavenging of charges by QDs (Fig. 2B). However, when the separation s is decreased below 8 nm, the system has a tendency for aggregation and hence all studies are restricted to s ≥8 nm. A similar trend in the reduction of ζ-potential is observed for Au-SiO_2(5.6), Au-SiO_2(10.8) and Au-SiO_2(17.3) on addition of QDs (Tables S2-S5). It is found that the ζ-potential decreases linearly with the number density of CdSe/ZnS for all shell thicknesses (Fig. S7). The hybrid system holds a high positive surface charge even at the highest number density of QDs; e.g., a ζ-potential of +51.2 mV for s = 8 for Au(1.35). Based on these results, the possibility of unbound negatively charged CdSe/ZnS present in the solution is ruled out confirming our assumption. In covalently linked emitters bound on plasmonic systems, it is possible to separate the unbound chromophores by centrifugation. Attempts to rule out the possibility of any unbound QDs by centrifuging the solution containing the hybrid system, are not successful since a large amount of electrostatically bound CdSe/ZnS QDs tend to separate during the centrifugation (ESI).

PL intensity of CdSe/ZnS in the absence (I_0) and presence of AuNPs is monitored at the emission maxima of CdSe/ZnS (561 nm). The emission of CdSe/ZnS in the presence of plasmonic nanoparticles (I_{obs}) needs to be corrected (I_{corr}) for two wavelengths of the hybrid systems arises due to the primary and secondary inner filter effect (IFE), respectively. In the case of QD-bound plasmonic systems presented herein, IFE is all the more important due to the scavenging of both the incident light (primary IFE) and the emission from QDs (secondary IFE) by AuNPs (ε ~10^9 $M^{-1}cm^{-1}$; *vide supra*). As a result, the observed emission intensity will be less than the actual intensity and it is essential to apply correction factor (*CF*) to PL intensity.[61] Two independent methods have been undertaken to confirm the accuracy of the approach.

(i) CF for IFE - Method 1: This method, uses absorbance to correct for the IFE using eqn (1) as provided by Lakowicz.[62, 63]

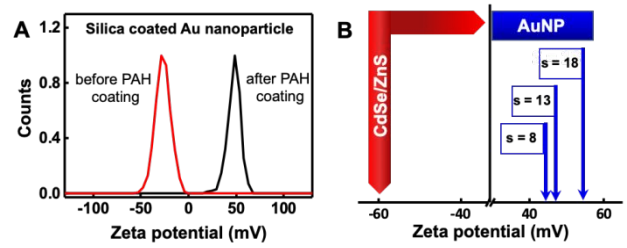

Fig. 2 (A) Zeta potential distribution of silica coated AuNPs before (red trace) and after PAH coating (black trace). (B) Zeta potential of Au(1.35) on addition of varying concentrations of CdSe/ZnS yielded QD-QD separations (s) of 8, 13, and 18 nm.

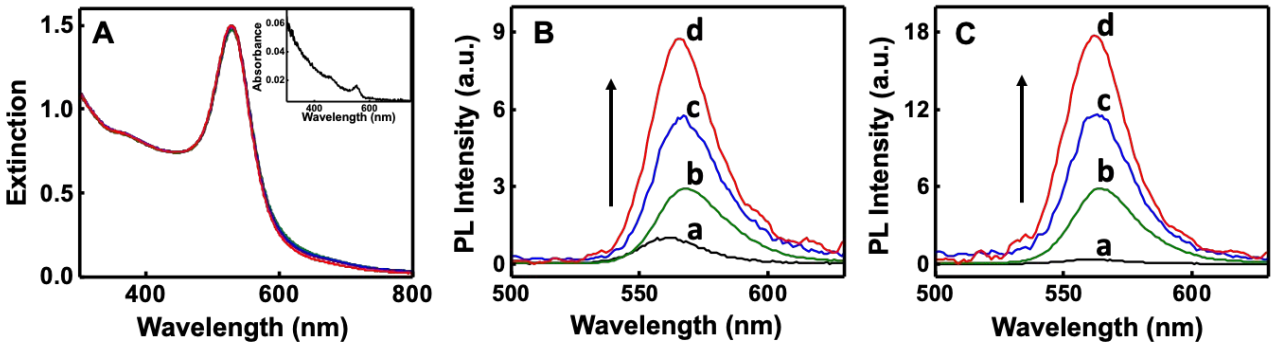

Fig. 3 (A) Extinction spectra of Au(1.35) in the absence and presence of CdSe/ZnS by varying the separation between the QDs (s = 8, 13 and 18 nm). The changes in extinction spectra on addition of CdSe/ZnS are negligible and hence the traces are not labelled. The inset shows the absorption spectrum of CdSe/ZnS used for s = 8 nm. (B) Trace (a): PL spectrum of CdSe/ZnS QDs; Trace (b-d): PL spectra of CdSe/ZnS QDs bound to Au(1.35) by varying the separation (s) between the CdSe/ZnS QDs as (b) 8, (c) 13, and (d) 18 nm. (C) Trace (b-d): Corrected PL spectra (IFEm1 and surface effect correction applied) of CdSe/ZnS QDs bound to Au(1.35) by varying the separation (s) between the CdSe/ZnS QDs as (b) 8, (c) 13, and (d) 18 nm. PL spectrum (IFE_{m1} applied) of CdSe/ZnS bound to SiO_2 NPs presented as trace (a) in C, used to determine surface effects (independent of variation of s; Table S6).

Absorbance at the excitation and emission wavelength causes an attenuation of PL intensity by a factor of $10^{0.5A_{ex}}$ and $10^{0.5A_{em}}$, respectively for a square cuvette having path length 1 cm where, A_{ex} and A_{em} represent the absorbance at the excitation wavelength (375 nm) and emission wavelength (561 nm), respectively. Therefore, the IFE by method 1 (denoted as IFE_{m1}) is given as

$$IFE_{m1} = 10^{(A_{ex} + A_{em})/2} \quad (1)$$

(ii) CF for IFE - Method 2 (cell shift method): A mathematical model based on measured fluorescence intensity is proposed by Patterson and co-workers.[64] In this model, dimensions of the interrogation zone which is the volume in which PL is collected by the instrument is incorporated. The effective width of emission (Δx) and excitation (Δy) beams are obtained by monitoring PL intensity as a function of displacement of cuvette in x- and y-directions by moving the cuvette on a translation stage (Scheme S2 and Fig. S9).[65] Experimental details are provided in the ESI. The IFE by method 2 (denoted as IFE_{m2}) is given as

$$IFE_{m2} = \frac{2.303A_{ex}\Delta x\, 10^{A_{ex}x_1}}{1-10^{-A_{ex}\Delta x}} \frac{2.303A_{em}\Delta y\, 10^{A_{em}y_1}}{1-10^{-A_{em}\Delta y}}, \quad (2)$$

where, x_1 and y_1 are the distances from inner wall of cuvette to the edge of beam in x- and y-directions, respectively.

(iii) CF for surface effects: Here we consider the emission changes on binding of QDs on nanoparticle surface in the absence of plasmonic field (Scheme 1C). The QDs showed a three-fold enhancement in the emission intensity in the presence of PAH coated silica nanoparticle (SiO_2 NPs) at all the separations and results are presented in the Table S6.

CF due to the environmental effect is accounted in all cases by dividing the PL intensity of the plasmonic hybrid system by a factor of three (*vide supra*). Further the corrections for IFE obtained by methods 1 and 2 are applied independently. In short, the emission intensity corrected for IFE and environment effects at a given wavelength is $I_{corr} = I_{obs} \times IFE/3$. Extinction spectra of Au(1.35) in the absence and presence of CdSe/ZnS by varying the separation between the QDs (s = 8, 13 and 18 nm) are presented as Fig. 3A and the corresponding PL spectra before and after applying the corrections for IFEm1 and surface effects in Fig. 3B,C. The extinction spectra (Figs. S4 and S5) and the emission spectra, before and after correction, for Au(1.35), Au-SiO_2(5.6), Au-SiO_2(10.8), Au-SiO_2(17.3) and SiO_2 NP at QD-QD separations of s = 8, 13 and 18 nm are provided in the ESI (Figs. S10-14). From the corrected spectra, the emission intensity at 561 nm is extracted and used for estimating the experimental enhancement factor $\left(\frac{I_{corr}}{I_0}\right)$. The experimental enhancement factor obtained by methods 1 and 2 (cell shift) are further denoted as $\mathrm{EF_{exp}}$ and $\mathrm{EF_{exp}(cs)}$, respectively. The $\mathrm{EF_{exp}}$ and $\mathrm{EF_{exp}(cs)}$ of CdSe/ZnS at various thicknesses from plasmonic nanoparticles are presented as Fig. 4 and S15, respectively. More importantly, the values obtained by applying methods 1 and 2, at different t and s, falls within the error limit thus establishing the reliability of both the methods. Hence for further discussion, experimental enhancement factor obtained using method 1 ($\mathrm{EF_{exp}}$) is used.

From the landscape of PL presented in Figure 4, it is evident that the experimental emission enhancement factor of CdSe/ZnS decreases with increase in t for all separations. The reduction in the $\mathrm{EF_{exp}}$ with distance from the plasmonic surface is attributed to the decrease in electric field experienced by the QDs. It is reported that the SERS signal[4,66] and emission enhancement[67-69] of various chromophoric molecules decreases with increase in distance from the plasmonic nanoparticles' surface due to the decay of electric field. The $\mathrm{EF_{exp}}$ of CdSe/ZnS also increases with increasing s on the surface of Au(1.35), Au-SiO_2(5.6), Au-SiO_2(10.8) and Au-SiO_2(17.3). For example, emission of CdSe/ZnS on the surface of AuNP at a spacer thickness, t ~ 1.35 nm is enhanced by 5.5-fold at shorter QD-QD separation of s = 8 nm (59 QDs/AuNP; Table S1) which increased to 17-fold when s = 18 nm (12 QDs/AuNP). The reduction in PL efficiency at shorter separation, i.e., higher QD number density on AuNP, is due to the interaction between QDs which are in close proximity on the plasmonic surface. At larger t such as in Au-SiO_2(17.3), the dependence of s on $\mathrm{EF_{exp}}$ is found to be minimal since the electric field effects are less dominant. These results confirm that the QD-QD interactions are plasmon assisted, further

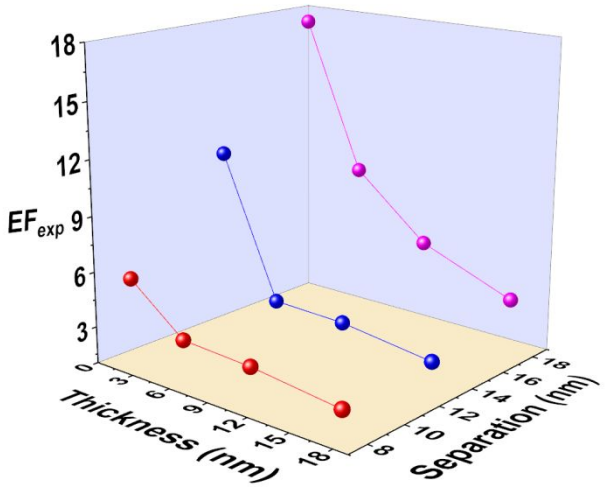

Fig. 4 3D-plot illustrating the enhancement of emission (EF_{exp}) of CdSe/ZnS by varying the spacer thickness (t) and QD-QD separation (s). Note: The extinction spectra of the CdSe/ZnS bound to Au(1.35), Au-SiO_2(5.6), Au-SiO_2(10.8) and Au-SiO_2(17.3) at different s values, overlaps with the extinction spectra of the corresponding plasmonic nanoparticles eliminates the possibility of aggregation (Fig. S4). 3D-plot illustrating $EF_{exp}(cs)$ of CdSe/ZnS by varying t and s is presented as Fig. S15.

supported by the fact that emission of CdSe/ZnS when bound on SiO_2 NPs is unaffected by the variation of s (Table S6).

Furthermore, we have investigated PL lifetimes of CdSe/ZnS bound on both SiO_2 NPs and plasmonic nanoparticles at various t (Figs. S16 and S17). In all the cases, a triexponential decay is observed: (i) a short-lived component, (ii) a component with intermediate lifetime and (iii) a long-lived component. It is well-established in the literature that the short-lived, intermediate and long-lived components correspond to hole trap, band edge and electron trap states, respectively.[70] Some interesting observation can be drawn from the intensity weighted average lifetimes (τ_{avg}) presented in Table S7. The τ_{avg} of CdSe/ZnS in water is 0.6 ns which increased to 0.97-1.07 ns when bound on SiO_2 NPs, attributed to surface effects. The τ_{avg} of CdSe/ZnS bound on SiO_2 NPs is more or less independent of QD-QD separation as observed in PL studies. In the present case, the τ_{avg} of CdSe/ZnS in plasmonic field at s = 18 nm is lower compared to QDs bound on SiO_2 NPs. The reduction in τ_{avg} of an emitter is indeed a characteristic behaviour of MEF. Interestingly, τ_{avg} of CdSe/ZnS increased with decrease in s, for all thicknesses, further indicates that the QD-QD interaction (crosstalk) is plasmon assisted. A plausible cause of the enhanced lifetime observed at the shorter separation (s = 8 nm) is plasmon assisted energy transfer between QDs.[71, 72] Energy transfer between QDs can occur due to the inhomogenous distribution of size present within the sample (Fig. S1). It is well established in the literature that the energy transfer processes exhibit a distance dependence; i.e, higher transfer efficiency at shorter distance.[62] Thus the increase in τ_{avg} of CdSe/ZnS in plasmonic field with decrease in s may be attributed to an enhanced energy transfer.

Based on the steady state and time resolved fluorescence studies, it is concluded that the decrease on PL enhancement observed at higher density of QDs, i.e., shorter s, at all thicknesses is due to plasmon assisted QD-QD interactions. The role of s on the emission behaviour have been explored by many groups. These include the (i) report by Murphy and co-workers on the quenching of emission of dye on the surface of AuNP coated with silica when s is <9 nm (t = 33 nm) as Förster resonance energy transfer (FRET);[31] (ii) fluorescence quenching of Atto 532 dye on the surface of silica nanoparticles by Mulvaney, Bach and co-workers as nonradiative energy transfer due to homo-FRET and existence of trap states,[43] and (iii) enhanced energy transfer between CdTe QDs of different size when proximal to AuNPs by Rogach and co-workers.[71] In the present case, when separation (s) between two emitters bound on Au(1.35) is 18 nm, number of CdSe/ZnS that can be placed on the surface is twelve. On further decreasing the number of QDs, the PL counts drop below the detection limit resulting in a noisy spectrum and hence not investigated. These aspects are further explored theoretically by placing point dipole emitters in plasmonic field of AuNP by varying s and t. However, at larger t and small s, the number of QDs loaded on plasmonic surface become large, hence challenging to model theoretically.

Electrodynamics Modelling. For the QDs/AuNP systems, our experiments can involve N ≈ 12-200 QD emitters (depending on shell thickness, t, and average separation, s, between neighbouring QDs) around the nanoparticles. Furthermore, the orientations of the emitter dipoles and the realistic interactions between them beyond elementary point-dipole interactions are not easily determined. While quantitative modelling of such systems is therefore challenging, it is interesting to examine the predictions of classical electrodynamics calculations based on idealized models of our hybrid systems. Briefly, we carry out classical electrodynamics calculations of spherical core-shell systems with N point dipole emitters distributed around the shell. The positions of the emitters are determined from solutions of the Thomson problem[56], i.e., they are chosen to minimize Coulombic repulsion. We also considered various orientations of the point dipoles such as perpendicular and parallel orientations relative to the nanoparticle surface and simple orientational averages, e.g., one third of the sum of the perpendicular and twice the parallel orientation results. The electromagnetic fields are found with a generalized multiparticle Mie theory or aggregate T-matrix method[73] for which there is an efficient Python package.[74] From these fields, we determine the radiative and nonradiative enhancements, f_r and f_{nr} relative to the dipoles in the absence of the core-shell nanoparticle (see also ESI).[75,76] If we define $f_t = f_r + f_{nr}$, as the normalized total rate, then the fluorescence enhancement (or possibly quenching) factor, EF_{theor}, is given by,[77]

$$EF_{theor} = F_{ex}\, F_{em}, \qquad (5)$$

and is a product of an electric field (E) enhancement factor at the excitation wavelength, λ_{ex},

$$F_{ex} = \left(\frac{|E|^2}{|E_0|^2}\right)_{\lambda_{ex}}, \qquad (6)$$

and a factor

$$F_{em} = \left(\frac{f_r}{\eta(f_t - 1) + 1}\right)_{\lambda_{em}}, \quad (7)$$

evaluated at the emission wavelength, λ_{em}. This latter term also involves the intrinsic quantum yield for the quantum dots, $\eta = \frac{k_r^0}{k_r^0 + k_{nr}^0}$, with k_r^0 and k_{nr}^0 being radiative and nonradiative decay rates for the QDs in the absence of the AuNP. Note that only when $|\eta(f_t - 1)|$ << 1 does eqn (5) correspond to the simple expectation of the overall enhancement being the product of the electric field enhancement factor and the radiative rate enhancement factor. See the ESI for additional technical details of our calculations.

Theoretical Results for Model Systems. *The N = 0 and 1 cases.* The cases of no or one QD on the AuNP are important to set the base picture. Analytical solutions[78] also exist for these cases that can be used to gauge the quality of our numerical methods and we have verified that our numerical solutions agree with the analytical ones. We have also verified that the theoretical and experimental extinction spectra matches well (Fig. S18). Fig. 5 presents the electric field enhancement factor, F_{ex}, evaluated at λ_{ex} = 375 nm. We evaluate this latter factor at a point on where a QD emitter could imagine to be placed at consistent with a shell thickness of t = 1.35 nm. More specifically, if the AuNP is centred at the origin, we evaluate F_{ex} at the Cartesian position x = $d_{Au}/2$ + t + $d_{QD}/2$, with y = z = 0, which is where one would imagine the dipole to be placed. Two incident light polarization cases are considered: (i) along x, which would induce the dipole to oscillate perpendicular to the AuNP surface and (ii) along y, which would induce the dipole to oscillate parallel to the AuNP surface. As can be seen, the perpendicular case leads to enhancements on the order of five at the smallest positions considered (consistent with spacer thickness t = 1.35 nm), but the parallel case can actually lead to some degree of quenching ("cold spots").[79] The reason why the best electric field enhancement factor is only on the order of five is that the excitation wavelength is 150 nm lower than the AuNP's plasmon resonance as indicated in Fig. 3A. Figs. 6A and 6B result from the calculations that do place a single dipole emitter at a position consistent with a spacer thickness t = 1.35

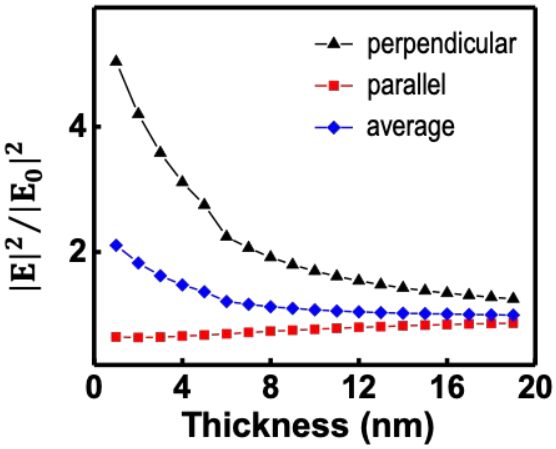

Fig. 5 Electric field intensity enhancement, F_{ex}, as a function of thickness (t) of a spacer layer from the Au nanoparticle surface having a 33 nm diameter, evaluated at λ_{ex} = 375 nm. For fixed t, we considered two cases of incident polarization, perpendicular and parallel, as defined in the text.

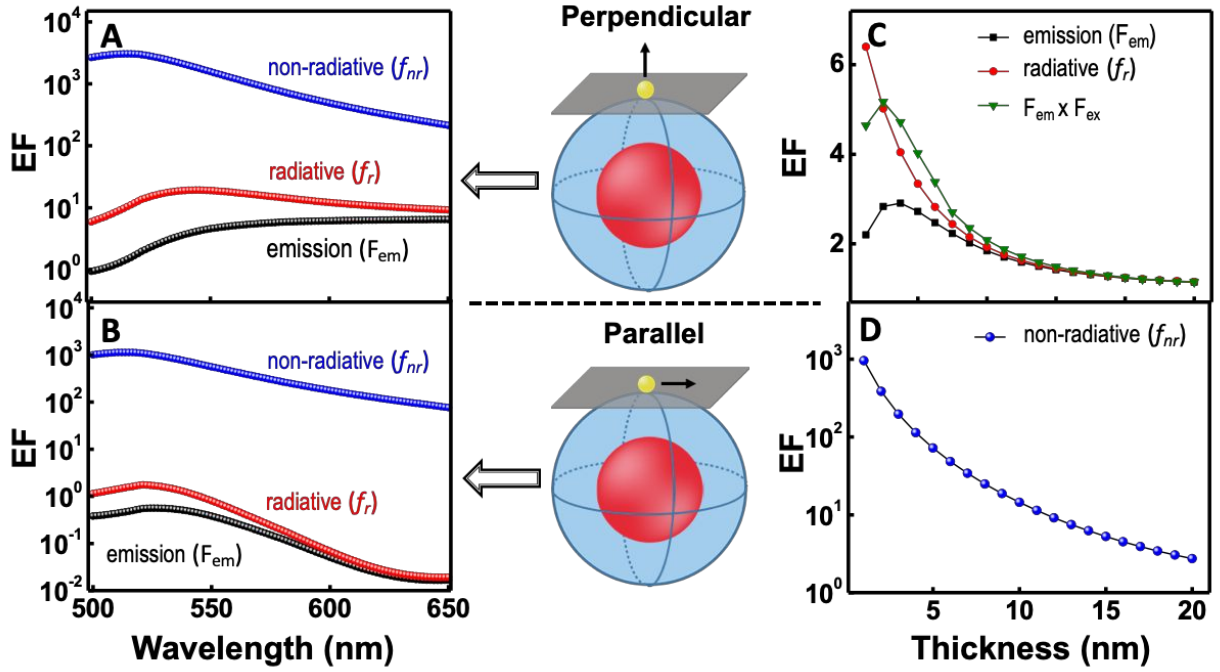

Fig. 6 (A,B) The various enhancement factors for the case of a single dipole emitter, assuming it is oriented, i.e., oscillating (A) perpendicular to the AuNP surface and (B) parallel to the AuNP surface, with a fixed t = 1.35 nm and varying the imagined emission wavelength. (C,D) The N = 1, orientationally averaged enhancement factors as a function of spacer thickness, t, with emission wavelength fixed at 561 nm. In (C), the overall enhancement factor is also shown (green triangles and lines), which accounts for the enhancement both at excitation and through emission, eqn (5), as well as just the radiative contribution, f_r (red circles and lines) and the emission enhancement (black squares and lines), eqn (7). (D) The normalized nonradiative rate. Illustration of the orientation of point dipole of the emitter on plasmonic surface having a spacer is shown in the middle column. The blue, red and yellow colors represent spacer, plasmonic material and emitter, respectively.

nm, and correspond to the enhancement factors, as a function of emission wavelength. For the calculation of F_{em}, we have assumed an intrinsic quantum yield factor, η = 0.002, inferred from our experiments (ESI). Fig. 6A represents the dipole being oriented (i.e., having a non-zero component) perpendicular to the AuNP's surface and Fig. 6B represents a parallel orientation of the dipole. Because the dipole is relatively close to the AuNP surface, the normalized nonradiative rate, f_{nr}, is quite large and leads to large values of the total rate enhancement, f_t, seen in both Figs. 6A and 6B. The overall enhancement factor due to emission, F_{em}, as a consequence, is somewhat smaller than the radiative enhancement factor, f_r. For the perpendicular dipole case, at an emission wavelength of λ_{em} = 561 nm, F_{em} = 5.3, about three times smaller than the corresponding f_r. In the parallel case, at this same emission wavelength, we actually see quenching: F_{em} = 0.22.

We present N = 1 fluorescence enhancement results as a function of spacer thickness, t, focusing on just λ_{em} = 561 nm in Figs. 6C and 6D. Fig. 6C also includes the overall enhancement factor, EF_{theor}, calculated from eqn (5) that includes the electric field enhancement factor (green curve). From Fig. 6C we see that the largest (averaged) EF values are on the order of 4-5 for t = 1.35 nm. By t = 10 nm, *EF* is approximately 2 and by t = 20 nm, it is about 1.1. This general trend of decreasing *EF* with t is consistent with our experimental results. Fig. 6D indicates that the normalized nonradiative rate can be quite large for small t.

The experimental case corresponding to average QD separations of s = 18 nm in Fig. 4 is likely close to the N = 1 limit because QD-QD interactions should be relatively small. Overall EF factors for N = 1 are also displayed in the lower panel of Fig. 7 and compared with experimental enhancement factor (EF_{exp} and ($EF_{exp}(cs)$) obtained by applying IFE corrections. Both theory and experiment show the same trend of increased enhancement with decreasing thickness for comparable thickness values, although theory has a maximum near t = 2 nm and a slight decreasing trend is evident. Note that the experimental enhancement factors are actually nearly four times larger than the theoretical ones as seen in lower panel of Fig. 7. The theoretical electric field enhancement factors at the excitation wavelength of 375 nm and the emission wavelength of 561 nm are also displayed (upper panel of Fig. 7), as well as the product of these two enhancements (filled triangles). At a simple level one might expect *EF* to scale with this latter product, although we see from the lower panel of Fig. 7 that it does not (filled triangles). This is likely due to the increased importance of nonradiative contributions to *EF* as t is decreased that we have already noted (Fig. 6D).

Theoretical results on increasing the number of QDs, N. Fig. 8 depicts the average nearest neighbour separation, s, and how it depends on N, the number of quantum dots, inferred from our Thomson problem geometries. Several representative Thomson geometries for low N are also displayed (Fig. 8B). It is challenging for us to carry out calculations for many of the experimental conditions, e.g., experimental case having s = 8 nm and t = 17.3 nm involves over 200 QDs and furthermore, we have found that the results are also sensitive to dipole orientations. However, we can look at N in the [1, 25] range and

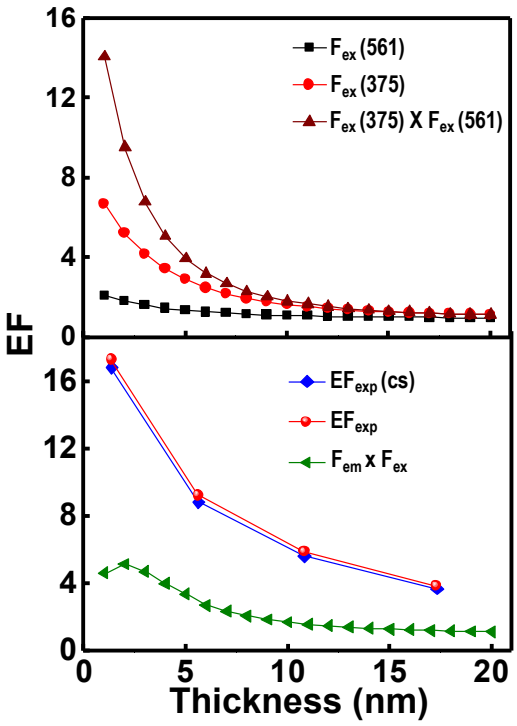

Fig. 7 The top panel display average electric field intensity enhancement at the excitation wavelength (375 nm) marked as filled circles and the average electric field enhancement at the emission wavelength (561 nm) as filled squares. The product of these to intensity enhancements is shown as filled triangles. The lower panel displays the effect of variation of spacer thickness (t) on the experimental PL enhancement factors (EF_{exp} as red filled circles and $EF_{exp}(cs)$ as blue filled diamonds), compared with electrodynamics-based N = 1 model (filled green triangles).

focus on trends for the simple average over three polarizations discussed in the Theoretical Methods section.

Fig. S19 presents the results for t = 1.35 nm (top panel) and t = 5.6 nm (bottom panel). We see from Fig. S19 that in the low N region, F_{em} is highest and is then a decreasing function of N, eventually reaching a plateau in the N = 10-20 range for both cases. From Fig. 8A we see that, for a given t (curve), as N increases, s decreases. Our theoretical results are also consistent with recent electrodynamics calculations on the effects of multiple point dipoles around metal NPs that have seen, as N is increased, plateauing and relatively small fluorescence enhancements in the N = 6-10 range.[44, 80] Reinterpreted in terms of average nearest QD separations, s, we can say that F_{em} will be flat at low s values and then increase with increasing s, which is qualitatively consistent with our experiments. Keeping in mind that F_{ex} is about a factor of two larger for t = 1.35 nm than t = 5.6 nm we conclude that at low N the overall enhancement factor, eqn (5), will be larger for the t = 1.35 nm case, which is again qualitatively consistent with experiment (Fig. 4). It is interesting to note that, as with the N = 1 case, the normalized nonradiative rate is quite large in both cases but tends to decrease and plateau with increasing N. As expected, this factor, while still significant, is smaller for t = 5.6 nm compared to t = 1.35 nm.

Despite qualitative agreement between theory and experiment in terms of trends, there are quantitative discrepancies

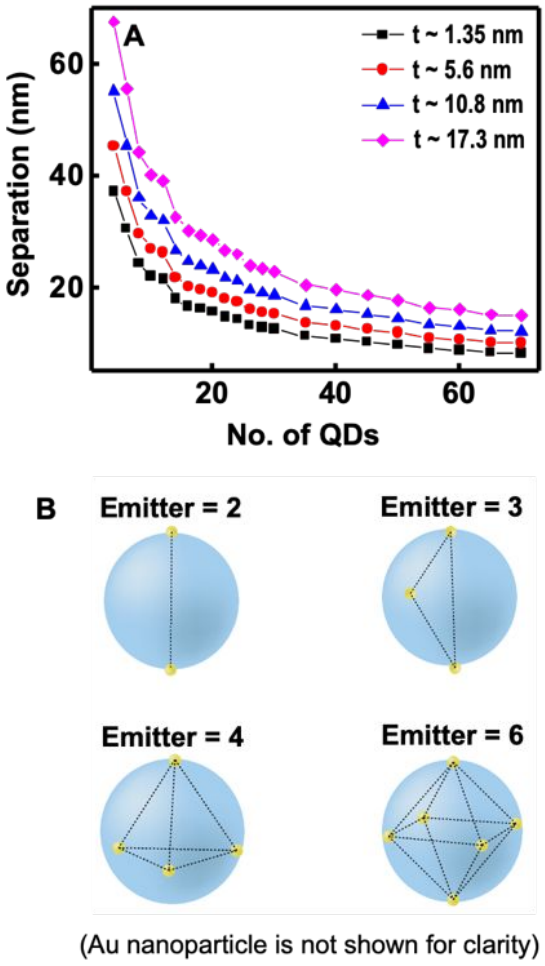

Fig. 8 (A) Average nearest-neighbour separations, s, between QDs in QDs/AuNP systems as a function of the number of QDs on top of the silica shell of thickness ranging from t = 1.35 to 17.3 nm, estimated theoretically based on Thomson problem. (B) Representative Thomson geometries for N = 2, 3, 4 and 6. The emitter (yellow) on Au nanoparticle with spacer (blue). Note: Au nanoparticles are not shown for clarity.

between the theoretical enhancement factors in Fig. S19 and our experimental results (Figs. 4 and S15). Most significantly, the experimental results do not plateau for the smallest values of s (largest N) considered. At t = 1.35 nm, for example, EF_{exp} decreases by a factor of two between s = 13 nm (N = 23) and 8 nm (N = 59) and yet the theoretical result (Fig. S19, top panel) is relatively flat for all N > 10. Another discrepancy is the general magnitude of the enhancements, with the theoretical ones being smaller than the experimental ones. For example, taking the average value of the field enhancement factor from Fig. 5B at t = 1.35 nm of $F_{ex} \approx 2$, the largest $\mathrm{EF_{theor}} = F_{ex}F_{em} \approx 2 \times 2.5 = 5$, whereas the largest experimental result from Fig. 4 is 17.

To conclude our theoretical discussion, we have found that it is possible to verify the trends in s and t consistent with experiment using the canonical electrodynamics picture used for understanding MEF, i.e., point dipoles around a plasmonic nanoparticle. However, there are several reasons behind the quantitative discrepancies. It is highly unlikely that all the emitters will be excited and emitting at the same time in the experiments, which is an assumption in our model. A second reason is that the QDs may require a more sophisticated model beyond point-dipole to properly include both their interactions among themselves and with the nanoparticle (e.g., include a finite size and complex polarizability, multi-exponential decay dynamics and so on). A third reason is that a more thorough treatment of orientational averaging may be required and, related, is the fact that possibly other configurations than those consistent with the Thomson problem should be considered. Another possible source of theory/experiment disagreement is that the theory does not account for inhomogeneities (e.g., size distribution) in the QDs. These inhomogeneities will affect different QD-QD and QD-AuNP coupling strengths and thus non-radiative and radiative rates. Finally, at very small emitter-nanoparticle distances, quantum effects including nonlocal dielectric response and electron spill-out can become important considerations.[30, 81]

Conclusions

QD bound plasmonic nanohybrids are designed by electrostatically binding negatively charged CdSe/ZnS on Au nanoparticles coated with an inert shell having positive surface charge. Previous investigations on the enhancement of emission properties of an emitter in plasmonic field have been carried out by either varying distance between the plasmonic surface and emitter (t), or separation between the emitters (s) on metal nanoparticles' surface. However, the PL enhancement is indeed interdependent on s and t. Herein, we have simultaneously varied s and t to obtain the landscape of PL enhancement, which is first of its kind. The plasmon to emitter distance is tuned by increasing the thickness of the inert shell and varied the separation between the QDs on surface by changing the number density of CdSe/ZnS. Experimental studies presented in Fig. 4 conclude that the enhancement of PL of CdSe/ZnS when kept in plasmonic field is highly dependent on both s and t. More specifically, the EF_{exp} is large when (i) emitter is close to the plasmonic surface and (ii) the emitter-emitter interaction is minimum. For example, a seventeen-fold enhancement of PL is observed experimentally when t is ~1.35 nm and s is ~18 nm on placing CdSe/ZnS in the presence of Au nanoparticle (diameter ~33 nm). From the landscape of the experimental enhancement factor as a function of t and s (Fig. 4 and S15), it is clear that the crosstalk between the QDs in plasmonic field, at shorter s, results in a reduction in PL efficiency. Electrodynamics calculations of a simple model qualitatively follows the experimental trend of decreasing enhancement factor with increase in t and N. Our model of classical point dipoles emitting coherently is the simplest extension of the generally successful and much-used model for a single emitter interacting with a plasmonic system. The quantitative discrepancies between these calculations and experiment, point to the need of more sophisticated theoretical treatments when considering multiple-emitter problems as outlined at the end of the previous section. The results presented herein on PL enhancement of emitter in plasmonic field unambiguously corroborate the need of considering

emitter-emitter and emitter-plasmonic surface separations while designing hybrid systems with enhanced brightness.

Experimental

Materials. All the chemicals are used as obtained and details are provided in the ESI. All solvents used (hexane, methanol, isopropanol and acetone) are HPLC grade and poly(allylamine hydrochloride) having an average molecular weight of 17,500 is used for coating. All photophysical studies are carried out using double distilled water.

Instrumental methods. All photophysical studies are carried out at room temperature in quartz cuvette having a path length of 1 cm (Starna, USA). Absorption spectra and emission spectra are recorded on Shimadzu UV-3600 UV-vis-NIR spectrophotometer and Horiba Jobin Yvon-Fluorolog 3 spectrofluorimeter, respectively. Samples are excited using 450 W Xenon lamp and PL is detected using photomultiplier tube (180-850 nm). All steady-state PL measurements are carried out by exciting the sample at 400 nm with excitation and emission slit width as 2 nm. Samples for TEM are prepared by drop-casting the solution on 400 mesh carbon coated Cu-grid and the solvent is allowed to evaporate. Plasmonic nanoparticles are characterized using FEI Tecnai G2 Spirit Bio-Twin transmission electron microscope operating at an accelerating voltage of 120 kV. CdSe/ZnS are characterized using FEI Tecnai G2 F30 S -Twin TEM operating at 300 kV. Zeta potential measurements are carried out using Zetasizer Nanoseries (M3-PALS) Malvern-ZEN 3600. All the reported zeta potential values are the average of six independent measurements.

Synthesis of plasmonic nanoparticles. *Synthesis of gold nanoparticles*: We have adopted a kinetically controlled seed mediated method for the synthesis of citrate stabilized Au nanoparticles originally developed by Bastus et al.[82] AuNP seed is synthesized by reducing $HAuCl_4$ using trisodium citrate dihydrate (TSC). Particles of desired size are obtained by reducing $HAuCl_4$ on the surface of previously prepared seeds. In the first step (Step 1), a solution of TSC in water (2.2 mM; 150 mL) is boiled for 15 min in a round bottom flask and $HAuCl_4$ (25 mM; 1 mL) is added to the solution kept at 100 °C under vigorous stirring. The reaction is continued at the same condition for 15-20 min for the growth of the seed. Au nanoparticles of larger size are prepared by the addition of $HAuCl_4$ to the above seed solution in the presence of TSC at 90 °C. In the second step (Step 2), $HAuCl_4$ (25 mM, 1 mL) is added twice to the reaction mixture containing Au seeds with an interval of 30 min keeping the solution at 90 °C. The solution is kept for another 30 min at the same temperature, allowing the growth of the particle and 55 mL of the formed nanoparticle solution is removed from the RB flask. In the third step (Step 3) double distilled H_2O (53 mL) and TSC (60 mM, 2 mL) is added to the reaction mixture kept in the RB flask. After attaining a temperature of 90 °C, Steps 2 and 3 are repeated twice followed by Step 2. The nanoparticles are purified by centrifugation. The residue obtained is redissolved in double distilled water and stored.

The nanoparticles are further stabilized using polyvinylpyrrolidone (PVP) polymer. Aqueous solution of PVP (75 mg; 3 mL) is added to Au nanoparticle (30 pM, 150 mL) solution in water, under vigorous stirring (note: concentration of nanoparticle is estimated using UV-vis-studies). The reaction is allowed to continue for 15 h and purified by centrifugation.

Silica coating of gold nanoparticle: Au nanoparticles are suspended in a mixture (1:9) of water and isopropanol. Tetraethylorthosilicate (80 μL) is added to the nanoparticle solution after making it ammoniacal (30% ammonia solution; 0.5 mL) under vigorous stirring. Various shell thicknesses are obtained by controlling the reaction time. A red-shift in the extinction maxima is observed for gold nanoparticle upon silica coating (Fig. S2C).

PAH capping of nanoparticles: Bare Au nanoparticles and silica coated Au nanoparticles are further coated with polyallylamine hydrochloride (PAH). PAH (2 mg/mL) is dissolved in aqueous NaCl (2 mM) and sonicated for 30 min. Silica coated gold nanoparticles/gold nanoparticles in water is added dropwise to the above solution under vigorous stirring and further the reaction is allowed to continue for 3 h at low stirring speed. The nanoparticles are purified by centrifugation and redissolved in water.

Synthesis of SiO_2 NP. Silica nanoparticles without a plasmonic core is used as a reference substrate and synthesized using modified Stöber condensation reaction.[60] In a typical synthesis, tetraethyl orthosilicate (600 μL) is added dropwise to a mixture (1:9) of water and isopropanol (54 mL; contains 1 mL of 30% NH_4OH), under vigorous stirring for 2 h and centrifuged. The residue obtained is purified by repeated washing with water and centrifugation. The purified silica nanoparticles are stored by suspending in water (5 mL) which is used as the stock solution. The surface charge of the bare silica nanoparticle is negative due to the presence of hydroxyl groups and made positive by coating with the polyelectrolyte, PAH. This is achieved by slowly adding 3 mL silica nanoparticle (from the above stock solution) to a solution of PAH (90 mg) containing NaCl (2 mM) in water (45 mL).

Synthesis of cysteine capped CdSe/ZnS. *Synthesis of CdSe/ZnS in organic medium*: CdSe QDs capped with tetradecylphosphonic acid (TDPA), and trioctylphosphine oxide (TOPO) are synthesized by following a reported procedure with slight modification.[83] For the synthesis of CdSe QDs, Cd-TDPA complex is prepared by heating CdO (0.40 mmol), TDPA (0.80 mmol) and TOPO (6.46 mmol) at 300 °C in a three-necked round bottom flask kept under nitrogen. Selenium precursor prepared separately by dissolving selenium (0.4 mmol) in TOP (2.24 mmol) is injected to the above solution at 300 °C. The desired crystal size is obtained by adjusting the reaction time and temperature. The reaction is arrested by cooling down to room temperature by the immediate removal of the heating source. The nanocrystals formed are purified by repeated precipitation with methanol to remove the excess ligands and the starting materials. The final residue is re-dispersed in toluene and used for further synthesis and studies. The concentration of CdSe is estimated using absorption spectroscopic studies (ε at 556 nm = 2.00 x 10^5 $M^{-1}cm^{-1}$).

Overcoating of CdSe nanoparticles with ZnS is done using a modified procedure wherein zinc oleate, and octane thiol is used as the zinc and sulphur precursors, respectively.[84] CdSe QDs (30 nmol) are taken in a mixture of octadecene (1 mL) and trioctylamine (1 mL) and degassed for 1 h at 100 °C. Zinc oleate (43 μmol) and octane thiol (64 μmol) is further added to the reaction pot and then heated to 310 °C for 5 min. Then the nanocrystals are dissolved in hexane and precipitated with methanol and redispersed in toluene (15 mL) for phase transfer. *Phase transfer of CdSe/ZnS*: CdSe/ZnS capped with long alkyl chain ligands (TDPA and OA) is phase transferred to aqueous solution by precipitation method.[85] L-Cysteine (2 mmol) is dissolved in methanolic KOH solution (2 mL) and added to CdSe/ZnS in toluene (3 mL) and stirred for 5 min. On addition of methanolic ligand solution, QD precipitate out and thiol group in cysteine binds to CdSe/ZnS surface. The precipitate is collected by centrifugation and re-dissolved in double distilled water and further centrifuged to eliminate any solid impurities present. The concentration of CdSe/ZnS is estimated using absorption spectroscopic studies (ε at 551 nm = 1.92 x 10^5 $M^{-1}cm^{-1}$).

Author Contributions

The experiments are designed by K.G.T and E.M.T, and carried out by E.M.T together with L.P and form the part of the doctoral thesis of E.M.T. The theoretical studies are designed and carried out by S.K.G. and C.L.C. All authors contributed in the analysis and writing of the manuscript.

Conflicts of interest

There are no conflicts to declare.

Acknowledgements

Authors (K.G.T., E.M.T., L.P.) thank the Nanomission project (DST/NM/TUE/EE-01/2019) of the Department of Science and Technology (DST), Government of India for financial support. K.G.T. acknowledges the J. C. Bose National Fellowship of DST, Government of India. E.M.T. and L.P. acknowledge the fellowship from the Council of Scientific and Industrial Research, Government of India and IISER TVM, respectively. We thank John A. Parker for valuable advice on the electrodynamics calculations. Use of the Center for Nanoscale Materials, an Office of Science User Facility, was supported by the U.S. Department of Energy, Office of Science, Office of Basic Energy Sciences, under Contract No. DE-AC02-06CH11357.

Notes and references

1. K. D. Piatkevich and V. V. Verkhusha, in *Methods in Cell Biology*, eds. Z. Darzynkiewicz, E. Holden, A. Orfao, W. Telford and D. Wlodkowic, Academic Press, Cambridge, 2011, vol. 102, pp. 431-461.
2. S. Liu, H. Ou, Y. Li, H. Zhang, J. Liu, X. Lu, R. T. K. Kwok, J. W. Y. Lam, D. Ding and B. Z. Tang, *J. Am. Chem. Soc.*, 2020, **142**, 15146-15156.
3. J.-F. Li, C.-Y. Li and R. F. Aroca, *Chem. Soc. Rev.*, 2017, **46**, 3962-3979.
4. R. Thomas, A. Thomas, S. Pullanchery, L. Joseph, S. M. Somasundaran, R. S. Swathi, S. K. Gray and K. G. Thomas, *ACS Nano*, 2018, **12**, 402-415.
5. M. Achermann, *J. Phys. Chem. Lett.*, 2010, **1**, 2837-2843.
6. R. K. Yadav, M. R. Bourgeois, C. Cherqui, X. G. Juarez, W. Wang, T. W. Odom, G. C. Schatz and J. K. Basu, *ACS Nano*, 2020, **14**, 7347-7357.
7. R. Thomas, J. Kumar, J. George, M. Shanthil, G. N. Naidu, R. S. Swathi and K. G. Thomas, *J. Phys. Chem. Lett.*, 2018, **9**, 919-932.
8. H. Nabika, M. Takase, F. Nagasawa and K. Murakoshi, *J. Phys. Chem. Lett.*, 2010, **1**, 2470-2487.
9. X. Li, P. D. McNaughter, P. O'Brien, H. Minamimoto and K. Murakoshi, *Phys. Chem. Chem. Phys.*, 2018, **20**, 14818-14827.
10. V. Giannini, A. I. Fernández-Domínguez, S. C. Heck and S. A. Maier, *Chem. Rev.*, 2011, **111**, 3888-3912.
11. D. Darvill, A. Centeno and F. Xie, *Phys. Chem. Chem. Phys.*, 2013, **15**, 15709-15726.
12. J.-E. Park, J. Kim and J.-M. Nam, *Chem. Sci.*, 2017, **8**, 4696-4704.
13. M. Pelton, *Nat. Photonics*, 2015, **9**, 427-435.
14. C. D. Geddes and J. R. Lakowicz, *J. Fluoresc.*, 2002, **12**, 121-129.
15. J. R. Lakowicz, K. Ray, M. Chowdhury, H. Szmacinski, Y. Fu, J. Zhang and K. Nowaczyk, *Analyst*, 2008, **133**, 1308-1346.
16. K. H. Drexhage, in *Progress in Optics*, ed. E. Wolf, Elsevier, North-Holland: Amsterdam, The Netherlands, 1974, vol. 12, pp. 163-232.
17. J. Langer, D. Jimenez de Aberasturi, J. Aizpurua, R. A. Alvarez-Puebla, B. Auguié, J. J. Baumberg, G. C. Bazan, S. E. J. Bell, A. Boisen, A. G. Brolo, J. Choo, D. Cialla-May, V. Deckert, L. Fabris, K. Faulds, F. J. García de Abajo, R. Goodacre, D. Graham, A. J. Haes, C. L. Haynes, C. Huck, T. Itoh, M. Käll, J. Kneipp, N. A. Kotov, H. Kuang, E. C. Le Ru, H. K. Lee, J.-F. Li, X. Y. Ling, S. A. Maier, T. Mayerhöfer, M. Moskovits, K. Murakoshi, J.-M. Nam, S. Nie, Y. Ozaki, I. Pastoriza-Santos, J. Perez-Juste, J. Popp, A. Pucci, S. Reich, B. Ren, G. C. Schatz, T. Shegai, S. Schlücker, L.-L. Tay, K. G. Thomas, Z.-Q. Tian, R. P. Van Duyne, T. Vo-Dinh, Y. Wang, K. A. Willets, C. Xu, H. Xu, Y. Xu, Y. S. Yamamoto, B. Zhao and L. M. Liz-Marzán, *ACS Nano*, 2020, **14**, 28-117.
18. A. I. Pérez-Jiménez, D. Lyu, Z. Lu, G. Liu and B. Ren, *Chem. Sci.*, 2020, **11**, 4563-4577.
19. M. Li, S. K. Cushing, Q. Wang, X. Shi, L. A. Hornak, Z. Hong and N. Wu, *J. Phys. Chem. Lett.*, 2011, **2**, 2125-2129.
20. Y. Chen, M. B. O'Donoghue, Y.-F. Huang, H. Kang, J. A. Phillips, X. Chen, M. C. Estevez, C. J. Yang and W. Tan, *J. Am. Chem. Soc.*, 2010, **132**, 16559-16570.
21. C. S. Yun, A. Javier, T. Jennings, M. Fisher, S. Hira, S. Peterson, B. Hopkins, N. O. Reich and G. F. Strouse, *J. Am. Chem. Soc.*, 2005, **127**, 3115-3119.
22. S. Barazzouk, P. V. Kamat and S. Hotchandani, *J. Phys. Chem. B*, 2005, **109**, 716-723.
23. N. Mondal and A. Samanta, *J. Phys. Chem. C*, 2016, **120**, 650-658.
24. S. S. E. Collins, E. K. Searles, L. J. Tauzin, M. Lou, L. Bursi, Y. Liu, J. Song, C. Flatebo, R. Baiyasi, Y.-Y. Cai, B. Foerster, T. Lian, P. Nordlander, S. Link and C. F. Landes, *ACS Nano*, 2021, **15**, 9522-9530.
25. E. Dulkeith, M. Ringler, T. A. Klar, J. Feldmann, A. Muñoz Javier and W. J. Parak, *Nano Lett.*, 2005, **5**, 585-589.

26. O. Kulakovich, N. Strekal, A. Yaroshevich, S. Maskevich, S. Gaponenko, I. Nabiev, U. Woggon and M. Artemyev, *Nano Lett.*, 2002, **2**, 1449-1452.
27. C. Rohner, I. Tavernaro, L. Chen, P. J. Klar and S. Schlecht, *Phys. Chem. Chem. Phys.*, 2015, **17**, 5932-5941.
28. R. Gill and E. C. Le Ru, *Phys. Chem. Chem. Phys.*, 2011, **13**, 16366-16372.
29. H. Mishra, B. L. Mali, J. Karolin, A. I. Dragan and C. D. Geddes, *Phys. Chem. Chem. Phys.*, 2013, **15**, 19538-19544.
30. P. Anger, P. Bharadwaj and L. Novotny, *Phys. Rev. Lett.*, 2006, **96**, 113002.
31. N. S. Abadeer, M. R. Brennan, W. L. Wilson and C. J. Murphy, *ACS Nano*, 2014, **8**, 8392-8406.
32. X. Ma, K. Fletcher, T. Kipp, M. P. Grzelczak, Z. Wang, A. Guerrero-Martínez, I. Pastoriza-Santos, A. Kornowski, L. M. Liz-Marzán and A. Mews, *J. Phys. Chem. Lett.*, 2011, **2**, 2466-2471.
33. J. R. Lakowicz, *Anal. Biochem.*, 2005, **337**, 171-194.
34. D. Lee, J. Lee, J. Song, M. Jen and Y. Pang, *Phys. Chem. Chem. Phys.*, 2019, **21**, 11599-11607.
35. S.-Y. Liu, L. Huang, J.-F. Li, C. Wang, Q. Li, H.-X. Xu, H.-L. Guo, Z.-M. Meng, Z. Shi and Z.-Y. Li, *J. Phys. Chem. C*, 2013, **117**, 10636-10642.
36. S. Khatua, P. M. R. Paulo, H. Yuan, A. Gupta, P. Zijlstra and M. Orrit, *ACS Nano*, 2014, **8**, 4440-4449.
37. Z. Zeng, S. Mizukami, K. Fujita and K. Kikuchi, *Chem. Sci.*, 2015, **6**, 4934-4939.
38. S. Talebzadeh, C. Queffélec and D. A. Knight, *Nanoscale Adv.*, 2019, **1**, 4578-4591.
39. J. Asselin, P. Legros, A. Grégoire and D. Boudreau, *Plasmonics*, 2016, **11**, 1369-1376.
40. G. Schneider, G. Decher, N. Nerambourg, R. Praho, M. H. V. Werts and M. Blanchard-Desce, *Nano Lett.*, 2006, **6**, 530-536.
41. J.-H. Choi, J. Lim, M. Shin, S.-H. Paek and J.-W. Choi, *Nano Lett.*, 2021, **21**, 693-699.
42. Y. Fu, J. Zhang and J. R. Lakowicz, *J. Am. Chem. Soc.*, 2010, **132**, 5540-5541.
43. P. Reineck, D. Gómez, S. H. Ng, M. Karg, T. Bell, P. Mulvaney and U. Bach, *ACS Nano*, 2013, **7**, 6636-6648.
44. Y. Zhou, G. Chen and S. Zou, *J. Phys. Chem. C*, 2021, **125**, 2531-2536.
45. N. Liu, B. S. Prall and V. I. Klimov, *J. Am. Chem. Soc.*, 2006, **128**, 15362-15363.
46. Y. Chen, K. Munechika, I. Jen-La Plante, A. M. Munro, S. E. Skrabalak, Y. Xia and D. S. Ginger, *Appl. Phys. Lett.*, 2008, **93**, 053106.
47. Y. Bian, S. Liu, Y. Zhang, Y. Liu, X. Yang, S. Lou, E. Wu, B. Wu, X. Zhang and Q. Jin, *Nanoscale Res. Lett.*, 2021, **16**, 90.
48. L. Trotsiuk, A. Muravitskaya, O. Kulakovich, D. Guzatov, A. Ramanenka, Y. Kelestemur, H. V. Demir and S. Gaponenko, *Nanotechnology*, 2019, **31**, 105201.
49. H.-H. Lin and I. C. Chen, *J. Phys. Chem. C*, 2015, **119**, 26663-26671.
50. B. Fu, J. D. Flynn, B. P. Isaacoff, D. J. Rowland and J. S. Biteen, *J. Phys. Chem. C*, 2015, **119**, 19350-19358.
51. Z. Zhou, H. Huang, Y. Chen, F. Liu, C. Z. Huang and N. Li, *Biosens. Bioelectron.*, 2014, **52**, 367-373.
52. D. Nepal, L. F. Drummy, S. Biswas, K. Park and R. A. Vaia, *ACS Nano*, 2013, **7**, 9064-9074.
53. D. Cheng and Q.-H. Xu, *Chem. Commun.*, 2007, 248-250.
54. K. Ray, R. Badugu and J. R. Lakowicz, *Langmuir*, 2006, **22**, 8374-8378.
55. P. K. Sudeep, S. T. S. Joseph and K. G. Thomas, *J. Am. Chem. Soc.*, 2005, **127**, 6516-6517.
56. W. J. M. Ridgway and A. F. Cheviakov, *Comput. Phys. Commun.*, 2018, **233**, 84-109.
57. J. R. G. Navarro and M. H. V. Werts, *Analyst*, 2013, **138**, 583-592.
58. T. J. Wax, S. Dey, S. Chen, Y. Luo, S. Zou and J. Zhao, *ACS Omega*, 2018, **3**, 14151-14156.
59. M. Shanthil, R. Thomas, R. S. Swathi and K. George Thomas, *J. Phys. Chem. Lett.*, 2012, **3**, 1459-1464.
60. W. Stöber, A. Fink and E. Bohn, *J. Colloid Interface Sci.*, 1968, **26**, 62-69.
61. S. Kumar Panigrahi and A. Kumar Mishra, *J. Photochem. Photobiol. C*, 2019, **41**, 100318.
62. J. R. Lakowicz, *Principles of Fluorescence Spectroscopy*, Springer Academic, New York, 3rd edn., 2006.
63. M. Kubista, R. Sjöback, S. Eriksson and B. Albinsson, *Analyst*, 1994, **119**, 417-419.
64. B. C. MacDonald, S. J. Lvin and H. Patterson, *Anal. Chim. Acta*, 1997, **338**, 155-162.
65. Q. Gu and J. E. Kenny, *Anal. Chem.*, 2009, **81**, 420-426.
66. G. Kumari, J. Kandula and C. Narayana, *J. Phys. Chem. C*, 2015, **119**, 20057-20064.
67. A. Wokaun, H. P. Lutz, A. P. King, U. P. Wild and R. R. Ernst, *J. Chem. Phys.*, 1983, **79**, 509-514.
68. N. Akbay, J. R. Lakowicz and K. Ray, *J. Phys. Chem. C*, 2012, **116**, 10766-10773.
69. A. I. Dragan, E. S. Bishop, J. R. Casas-Finet, R. J. Strouse, J. McGivney, M. A. Schenerman and C. D. Geddes, *Plasmonics*, 2012, **7**, 739-744.
70. Y. Gao and X. Peng, *J. Am. Chem. Soc.*, 2015, **137**, 4230-4235.
71. V. K. Komarala, A. L. Bradley, Y. P. Rakovich, S. J. Byrne, Y. K. Gun'ko and A. L. Rogach, *Appl. Phys. Lett.*, 2008, **93**, 123102.
72. C. R. Kagan, C. B. Murray and M. G. Bawendi, *Phys. Rev. B Condens. Matter*, 1996, **54**, 8633-8643.
73. Y.-l. Xu, *Appl. Opt.*, 1995, **34**, 4573-4588.
74. J. A. Parker, https://github.com/johnaparker/miepy).
75. M. Liu, T.-W. Lee, S. K. Gray, P. Guyot-Sionnest and M. Pelton, *Phys. Rev. Lett.*, 2009, **102**, 107401.
76. C. F. Bohren and D. R. Huffman, *Absorption and Scattering of Light by Small Particles*, John Wiley & Sons, Weinheim, 2008.
77. H. Wang and S. Zou, *RSC Adv.*, 2013, **3**, 21489-21493.
78. R. Ruppin, *J. Chem. Phys.*, 1982, **76**, 1681-1684.
79. M. Haggui, M. Dridi, J. Plain, S. Marguet, H. Perez, G. C. Schatz, G. P. Wiederrecht, S. K. Gray and R. Bachelot, *ACS Nano*, 2012, **6**, 1299-1307.
80. A. Wang and S. Zou, *J. Phys. Chem. C*, 2021, **125**, 16211-16219.
81. H. M. Baghramyan and C. Ciracì, *Nanophotonics*, 2022, **11**, 2473-2482.
82. N. G. Bastús, J. Comenge and V. Puntes, *Langmuir*, 2011, **27**, 11098-11105.
83. Z. A. Peng and X. Peng, *J. Am. Chem. Soc.*, 2001, **123**, 183-184.
84. K. Boldt, N. Kirkwood, G. A. Beane and P. Mulvaney, *Chem. Mater.*, 2013, **25**, 4731-4738.
85. T. Kodanek, H. M. Banbela, S. Naskar, P. Adel, N. C. Bigall and D. Dorfs, *Nanoscale*, 2015, **7**, 19300-19309.